Cracking of Cr-coated accident-tolerant fuel during normal operation and under power-ramping conditions

Kisik Hong[1], J.R. Barber[1], M.D. Thouless[1,2] and Wei Lu[1,2]

[1] *Department of Mechanical Engineering, University of Michigan, Ann Arbor, Michigan 48109*

[2] *Department of Materials Science & Engineering, University of Michigan, Ann Arbor, Michigan 48109*

Abstract

In this paper, an analysis is presented for the cracking of Cr-coated Zircaloy claddings proposed for use in accident-tolerant fuels (ATF). Tensile hoop stresses are induced in the coating by pellet-cladding interaction (PCI), which results from the fuel swelling under normal operation, or from additional thermal expansion of the fuel after power ramping. The hoop stress is limited by the stress relaxation associated with dislocation glide that dominates the thermal creep in the coating. The energy-release rate for crack channeling has also been calculated, and it increases almost linearly with the thickness of the coating. By comparing this energy-release rate with the toughness of Cr, we can develop a design map for the maximum coating thickness required to avoid fracture at different levels of ramped power. We also propose a design protocol for coatings based on a simplified fracture analysis, which allows existing PCI codes to be leveraged.

(August 12, 2019)

1. Introduction

The fuel rods in a pressurized-water reactor (PWR) operate within the oxidizing environment of the primary coolant. Oxidation of the cladding results in the complementary process of hydrogen formation, which precipitates within the cladding in the form of brittle hydrides. The mechanical degradation induced by the hydride precipitation makes the cladding more vulnerable to failure from pellet-cladding interaction (PCI) (Cox, 1990). This process of hydride formation becomes even more severe when the integrity of the oxide layer is damaged by cracking and spalling, which can occur under normal operation (Georgenthum *et al.*, 2006), or as a result of a reactivity-initiated accident (RIA) power transient (Hong *et al.*, 2018).

These problems have prompted the development of accident-tolerant fuel (ATF) claddings that are more resistant to oxidation. Several ATF technologies have been suggested; these include coated-Zircaloy, FeCrAl, and SiC/SiC (SiC fiber-reinforced SiC matrix composite) claddings (Terrani, 2018). The coated-Zircaloy cladding has an advantage over the other techniques because it does not require manufacturing a cladding with completely different materials. With its easy and economical fabrication, coated-Zircaloy claddings are considered to be a near-term option for deployment (Kim *et al.*, 2015b, 2015a; Terrani, 2018).

Several metals and alloys have been considered as potential candidates for coating materials that can form a protective layer against oxidation (Terrani, 2018). Among them, Cr exhibits excellent performance in terms of radiation stability (Tang *et al.*, 2017; Zinkle and Snead, 2014) and corrosion resistance, at both the low temperatures corresponding to normal operation, and at the high temperatures corresponding to a design-basis accident (DBA) (Bischoff *et al.*, 2018; Wu *et al.*, 2018).

The adhesion strength between Zircaloy and Cr has been investigated by *ex-situ* experiments using ring-compression and ring-tensile tests (Kim *et al*., 2015a). It was found that interfacial adhesion was retained, without any spalling or buckling-driven delamination, even at high compressive or tensile strains (up to 6 %). In addition, numerical analyses have been conducted to study the in-core performance of a coated cladding (Lee *et al*., 2017; Wagih *et al*., 2018). Lee *et al*. (2017) calculated the development of compressive stresses in the coating in the absence of PCI. They analyzed the effects of pressure, thermal expansion, irradiation-induced axial growth, and creep. More recently, Wagih *et al*. (2018) investigated the tensile stress generated within the Cr coating as a result of PCI during normal operation, and as a result of transient conditions.

These previous studies have focused on the stress evolution in the coating. However, analysis of possible fracture is also essential because Cr is a relatively brittle material (Yang *et al*., 2008). Fracture, in the form of channeling cracks, has been observed experimentally in a Cr coating on Zircaloy using a ring-tensile test (Kim *et al*., 2015a). This is of concern because, once a crack propagates to the Cr/Zircaloy interface, extremely localized oxidation, in the form of pitting corrosion, can occur in the Zircaloy near the crack tip, as has been shown in autoclave corrosion tests (Brachet *et al*., 2015). This further results in serious mechanical degradation of the cladding by hydride embrittlement.

In light of these observations, we have performed a fracture analysis of the Cr coating under normal operation, and under power-ramping conditions. A finite-element model that incorporates multiple deformation mechanisms, such as creep, thermal expansion, irradiation growth, and fuel swelling and sintering, has been developed. Since experiments have shown

good interfacial adhesion between Cr and Zircaloy (Kim *et al*., 2015a), we did not consider delamination, but focused on the channeling cracks that can be induced by tensile hoop stresses, using a fracture-mechanics approach. We anticipate that our model could be used to expand existing fuel performance codes, including those being developed by the Consortium for Advanced Simulation of Light Water Reactors (CASL) (Hales *et al*., 2016).

2. Finite-element model

A finite-element model was developed to calculate the stress state within the Cr coating. Then, the conditions for the propagation of channel cracks within the coating were calculated using linear-elastic fracture mechanics (LEFM).

2.1 Geometry and boundary conditions

A finite-element model of the fuel assembly, consisting of the fuel pellet and cladding, was developed using the commercial software, ABAQUS. Because of the strong adhesion between the materials, it was assumed that the coating layer was perfectly bonded to the Zircaloy. A simplified, 1D, axisymmetric model was considered, as shown in Fig. 1. The dimensions used in the model were based on typical PWR fuel rods. The thickness of the Cr coating can vary from a few micrometers to tens of micrometers (Park *et al*., 2016, 2015). Therefore, a parametric study of the effect of coating thickness was performed.

The initial gap between the outer surface of the pellet and the inner surface of the cladding was assumed to be 80 μm, and filled with helium. The contact between the pellet and cladding was modeled by a normal, hard contact to prevent penetration. The internal pressure

induced by the helium gas was assumed to be constant at 4 MPa, while the external pressure associated with the primary coolant was set to be 16 MPa (Johnson *et al*., 1982).

The system was assumed to be initially at 300 K. Upon start-up, a uniform power generation of 20 kW/m (typical for a PWR under normal operation (Rozzia *et al*., 2011)) was applied to the fuel pellet as a body heat-flux. The temperature of the external surface of the cladding was set to be constant at 600 K, corresponding to the coolant temperature. Power-ramping transients were considered by parametric studies of increasing the power to various levels above 20 kW/m. The transition from normal operation to a power-ramping condition was assumed to occur in the form of a step change in the power generation.

The thermo-mechanical properties, such as elastic modulus, specific heat, density, thermal conductivity, and thermal-expansion coefficient, for the UO_2 pellet and Zircaloy cladding were obtained from the MATPRO model (Siefken *et al*., 2001), and from Holzwarth and Stamm (2002) for the Cr coating. The temperature-dependent thermal conductivity of helium in the gap between the fuel pellets and cladding was also obtained from the MATPRO model (Siefken *et al*., 2001). Perfect thermal contact (temperature continuity) was assumed once the pellet and cladding came into contact.

2.2 Deformation mechanisms

We implemented the creep of Zircaloy in the finite-element calculations, using a mechanism-based model built upon decades of experimental data (Wang *et al*., 2013). The creep of UO_2 was implemented using the deformation-mechanism map of Frost and Ashby (1982). These models incorporate multiple creep mechanisms, including dislocation creep, diffusional

creep, and power-law creep, with creep strains being controlled by the von Mises effective stress. The grain sizes of Zircaloy and UO_2, which are needed for the creep calculations, were assumed to be 50 μm and 10 μm, respectively.

The creep of Cr was also implemented using the deformation mechanisms of Frost and Ashby (1982). However, the value quoted in this reference for the dislocation-glide parameter, τ_g, which is the shear strength at 0 K, corresponds to a grain size of 0.1 mm, while the grain size in the middle of the coating is expected to be much smaller at about 300 nm (Kim *et al*., 2015a). Since the grain size affects τ_g, its value, 1.11 GPa, was obtained from the Hall-Petch relationship (Hall, 1951; Petch, 1953) with parameters taken from Brittain *et al*. (1985).

We also included irradiation-induced deformations of Zircaloy and UO_2 in the calculation, incorporating models from BISON (Hales *et al*., 2016) and MATPRO (Siefken *et al*., 2001) for irradiation creep and growth of Zircaloy, and from MATPRO for irradiation creep of UO_2 (see Appendix A.1-A.3).

The swelling of the UO_2 pellet, which is induced by the accumulation of fission products within the pellet, was modeled based on the MATPRO model (Siefken *et al*., 2001). During early irradiation, the expansion of the fuel caused by swelling can be partially compensated by the fuel densification induced by irradiation sintering. We therefore also incorporated densification by implementing the model from MATPRO (Siefken *et al*., 2001) (see Appendix A.4). The amount of densification strongly depends on the total densification that can occur, denoted as $\Delta\rho_0$ in Eq. (A. 4), which is associated with the initial porosity of the fuel (DOE,

1993). We first set this value to zero corresponding to a high initial fuel density, and then increased the value to explore how it affects the results.

Oxidation of the Cr coating layer was neglected in the calculations, because it is almost negligible under the operating conditions of a PWR (Kim *et al*., 2015b, 2015a; Ševeček *et al*., 2018).

3. Development of stresses in the Cr-coating layer

3.1. Normal operation

For the case of normal operation, 3 operating cycles (1 cycle = 18 months) with a linear heat rate (LHR) of 20 kW/m were considered. Figure 2a shows the development of the hoop stress at the surface of a Cr coating that is 10 μm thick. As can be seen from Fig. 2b, the stress in the coating is essentially uniform, since the coating is much thinner than the cladding. Immediately upon start-up, the stress becomes highly compressive (around 1 GPa) owing to the external pressure from the primary coolant and the mismatch in the thermal strain. Creep results in a rapid relaxation of the stress, until a first plateau is reached when the shrinkage rate of the cladding in response to the pressure in the coolant matches the creep rate of Cr. Once the gap is closed, the cladding expands because of the fuel swelling, and the stress in the Cr coating becomes tensile until it reaches a second plateau at which the expansion rate of the cladding matches the creep rate of Cr.

During operation, fission gases are released from the fuel, which can increase the internal pressure within the fuel rod to a value near the coolant pressure (Williamson *et al*., 2012). We therefore considered the effect of increasing internal pressure up to 16 MPa, equivalent to the

external pressure. Separate calculations showed that this leads to a delayed initiation of PCI owing to reduced rate at which the cladding creeps down. Similarly, if the fuel densification, $\Delta\rho_0$, increases, it delays the onset of PCI. However, neither of these has a significant effect on the maximum hoop stress in the coating.

Thermal gradients within the fuel, generated during the initial start-up or after the onset of a power ramp, can lead to radial cracking and crack-induced relocation (Oguma, 1983). However, these would only produce local effects restricted to the inner surface of the cladding. For example, a companion study (Hong *et al*., 2019) has shown that cracked fuel leads to localized stress fields in the vicinity of fuel cracks, but their effect vanishes away from the point of contact. As a result, fuel cracks have negligible effect on the stress in the Cr coating. We also considered increase in the average contact pressure owing to fuel relocation, modeled as an overall increase of fuel diameter given in BISON (Hales *et al*., 2016), but its effect was found to be negligible.

By comparing the effects of different creep mechanisms in the finite-element calculations, we found that power-law creep dominates the stress relaxation, while the contribution of diffusional creep is relatively small. In particular, the effect of diffusional creep on the stress in the coating almost vanishes when the grain size is larger than 500 nm, a typical grain size experimentally observed near the surface of the coating layer (Brachet *et al*., 2015). Results for a range of coating thicknesses between 1 μm and 100 μm showed that the stress in the coating after three cycles was almost independent of its thickness.

We also ran a separate calculation without including irradiation-induced deformations of the Zircaloy and UO_2, and found that they do not affect the result. This suggests that the dimensional changes induced by irradiation are relatively small compared to those caused by other mechanisms, such as thermal creep.

3.2. Power ramping condition

To study the development of stress in the coating under power-ramping conditions, a power history with 2 cycles of normal operation (LHR = 20 kW/m, denoted as LHR_{normal}) followed by 12 hours of power ramp was implemented in the numerical model.

The evolution of the hoop stress at the surface of the coating is shown in Fig. 3a for a thickness of 10 μm, and a ramped power of (40 kW/m), designated as 2 LHR_{normal}. It can be observed that the stress increases sharply after the onset of a power ramp, as a result of the thermal expansion of the pellet. The stress reaches a maximum level almost immediately (within 1 minute after the onset of a power ramp), before decreasing as a result of creep in the Cr coating (dominated by power-law creep in this particular case).

Our interest lies in the possible fracture of the Cr coating, therefore, we focus on the maximum stress that is reached immediately after power ramping. The stress distribution in the cladding and coating at this time is shown in Fig. 3b. The stress in the coating is 1.4 GPa, much higher than that during normal operation. It was found that the maximum tensile stress in the coating after a power ramp is essentially independent of the coating thickness.

An increase in the power during a power ramp causes an immediate thermal expansion of the fuel pellet, leading to an elevated tensile hoop stress in the Cr coating. The ramped power is

known to be a key factor contributing to possible PCI failures (Cox, 1990; Penn *et al.*, 1977). Therefore, the effect of different levels of ramped power on the development of the hoop stress in the Cr coating was investigated. The result is plotted in Fig. 4a, which shows the evolution of the hoop stress after different power ramps. As expected, a higher ramped power results in a larger hoop stress within the coating. After quickly reaching a maximum, the stress decreases with time as Cr creeps. It was found that the stress relaxation is dominated by power-law creep at low ramped powers, but is dominated by dislocation glide at high ramped powers. Figure 4b shows the maximum hoop stresses in the coating at different levels of ramped power. The maximum hoop stress increases with ramped power, but becomes essentially independent of power when dislocation glide becomes the dominant mechanism for stress relaxation.

4. Fracture analysis of crack channeling in the Cr-coating layer

Since the Cr coatings exhibit a columnar grain morphology near the surface, it is likely that suitable initial flaws for crack channeling are an inherent feature of the system, as observed in Brachet *et al.* (2015). Therefore, we assumed that such flaws pre-existed in the coating, and focused our attention on whether they could propagate as channel cracks under the appropriate level of hoop stress. The crack-channeling analysis was performed conservatively by assuming the crack depth to be equal to the thickness of the coating. The energy-release rate was calculated from the work done by the tractions (equal to the coating stress, but with opposite sign) applied to the assumed cracked surface. The conditions for a crack to channel were then obtained by comparing the energy-release rate to the coating toughness.

The steady-state energy-release rate for crack channeling in a layer of thickness d is given by (Beuth, 1992)

$$\mathcal{G}_{ss} = \frac{1}{2}\frac{\sigma^2 d}{\bar{E}}\pi g(\alpha,\beta), \tag{1}$$

where σ is the tensile stress in the coating layer, given here by the maximum stress after the power ramp, $\bar{E}$ is the plane-strain modulus of the layer, and $g(\alpha,\beta)$ is a function of the Dundurs' bimaterial parameters α and β (Dundurs, 1969). For the material combination of Cr with Zircaloy, we have $\alpha = 0.56$ and $\beta = 0.14$, and $g(\alpha,\beta) = 2.26$. The energy-release rate was calculated using Eq. (1), which is plotted in Fig. 5 as a function of the coating thickness for different levels of ramped power.

With a body-centered-cubic structure, Cr exhibits a ductile-to-brittle transition temperature (DBTT) (Holzwarth and Stamm, 2002). This transition temperature decreases as the grain size increases, with a value of 660 K at a grain size of 34 μm and a value of 255 K at a grain size of 225 μm, respectively (Thornley and Wronski, 1972). Since even the smallest of these grains is bigger than those observed in the thin Cr coatings considered here, it is reasonable to assume that the operating temperatures of a PWR are much lower than the DBTT for Cr, so that a reasonable range for fracture toughness Γ is between 0.1 and 0.3 kJ/m^2 (Holzwarth and Stamm, 2002; Yang $et\ al$., 2008). This range is indicated by the hatched region in Fig. 5, with crack channeling occurring if $\mathcal{G}_{ss} > \Gamma$.

As mentioned in Section 3, the maximum tensile hoop stress for any given power history is almost independent of the coating thickness, at least up to 100 μm. Therefore, Eq. (1) indicates that the energy-release rate increases approximately linearly with the coating thickness. Figure 5 compares finite-element results (solid lines) with a linear approximation based on the maximum stresses for a 1 μm layer, for various power histories. The approximation differs

11

significantly from the more accurate results only in the ranges where the energy-release rate is well above the Cr fracture toughness. We shall exploit this result to develop a simpler fracture analysis protocol in Section 5.

By calculating the intersection between the lines of energy-release rate and toughness, one can obtain the critical coating thickness above which a channel crack forms. Figure 6 shows the critical thickness as a function of ramped power. The hatched region is associated with the range of fracture toughness, Γ, for Cr, with the lower bound corresponding to $\Gamma = 0.1$ kJ/m^2, and the upper bound to $\Gamma = 0.3$ kJ/m^2. The critical coating thickness decreases with increasing ramped power and reaches a plateau between 3 μm and 8 μm when dislocation glide becomes the dominant creep mechanism for stress relaxation. The Cr-coated Zircaloy cladding should be designed with the coating thickness in the safe zone, *i.e.*, less than the critical thickness of the coating.

These results may change quantitatively in that the actual properties of a Cr coating may differ from those assumed here, since they are taken from bulk values, and they may also vary depending on the fabrication technique, chemical composition, and grain size. However, it should be noted that the broad conclusions from the analysis are not affected by the detailed properties of the Cr coating. At the early stage of design, where *in-situ* experimental data are limited (Terrani, 2018), this analysis will be essential for constructing experiments to investigate the performance and for the actual design of the ATF cladding.

5. A simplified design protocol

The Cr coating is much thinner than the Zircaloy cladding. Therefore, the stress in the coating is dominated by its interaction with the cladding. This suggests a design protocol as follows:

1. Analyze the stress in the Zircaloy cladding, assuming no coating.

2. Impose the corresponding hoop strain with time on the Cr-coating layer.

3. Use the resulting hoop stresses in the coating layer to estimate the likelihood of channeling.

Step 1 can be achieved using existing PCI codes in the industry. The hoop stress in the coating can be computed in Step 2 by incorporating the creep mechanisms of Cr. In this way, one can easily perform cracking analysis of the Cr coating. We have confirmed through a simple Matlab routine (see Appendix B) that this protocol generated the same results of a full finite-element modelling of the cladding and coating together.

6. Conclusion

In this paper, the growth of channeling cracks in the Cr coated on Zircaloy cladding has been analyzed under normal operation, and under power-ramping conditions. It was found that high tensile hoop stresses develop in the coating when the cladding is pushed outwards through PCI. The maximum hoop stress increases with the ramped power, until the stress is limited by dislocation glide in the Cr coating.

The steady-state energy-release rate for crack channeling increases almost linearly with the thickness of the coating layer, allowing a critical coating thicknesses, above which cracking would occur, to be determined as a function of ramped power. This critical coating thickness

decreases with the level of ramped power. The design of Cr-coated Zircaloy cladding should ensure that the thickness of the coating layer is below the critical value. A design protocol has been suggested that allows fracture analysis of the Cr coating to be developed using existing PCI codes. This provides a design option without the need for developing new finite-element codes to analyze the cladding and coating layer together.

References

Beuth, J.L., 1992. Cracking of thin bonded films in residual tension. Int. J. Solids Struct. 29, 1657–1675.

Bischoff, J., Delafoy, C., Vauglin, C., Barberis, P., Perche, D., Duthoo, D., Schuster, F., Brachet, J.C., Schweitzer, E.W., Nimishakavi, K., 2018. AREVA NP's enhanced accident-tolerant fuel developments: Focus on Crcoated M5 cladding. Nucl. Eng. Technol. 50, 223–228.

Brachet, J.C., Le Saux, M., Le Flem, M., Urvoy, S., Rouesne, E., Guilbert, T., Cobac, C., Lahogue, F., Rousselot, J., Tupin, M., Billaud, P., 2015. On-going studies at CEA on chromium coated zirconium based nuclear fuel claddings for enhanced accident tolerant LWRs fuel. TopFuel 2015, Zurich, Switz. 31–38.

Brittain, C.P., Armstrong, R.W., Smith, G., 1985. Hall-Petch dependence for ultrafine grain size electrodeposited chromium. Scr. Mater. 19, 89–91.

Cox, B., 1990. Pellet-clad interaction (PCI) failures of zirconium alloy fuel cladding – a review. J. Nucl. Mater. 172, 249–292.

Dundurs, J., 1969. Discussion on "Edge-bonded dissimilar orthogonal elastic wedges under normal and shear loading." J. Appl. Mech. 36, 650–652.

DOE Fundamentals Handbook: Material Science. U. S. Dep. Energy, 1993.

Frost, H.J., Ashby, M.F., 1982. Deformation mechanism maps: the plasticity and creep of metals and ceramics. Pergamon Press.

Georgenthum, V., Desquines, J., Bessiron, V., 2006. Influence of outer zirconia transient cracking and spalling on thermomechanical behaviour of high burnup fuel rod submitted to RIA. J. Nucl. Sci. Technol. 43, 1089–1096.

Hales, J.D., Williamson, R.L., Novascone, S.R., Pastore, G., Spencer, B.W., Stafford, D.S., Gamble, K.A., Perez, D.M., Liu., W., 2016. BISON theory manual the equations behind nuclear fuel analysis, Technical Report INL/EXT-13-29930. Idaho National Lab.

Hall, E.O., 1951. The deformation and ageing of mild steel: III discussion of results. Proc. Phys. Soc. Sect. B 64, 747–753.

Holzwarth, U., Stamm, H., 2002. Mechanical and thermomechanical properties of commercially pure chromium and chromium alloys. J. Nucl. Mater. 300, 161–177.

Hong, K., Barber, J.R., Thouless, M.D., Lu, W., 2019. Effect of power history on pellet-cladding interaction. Nucl. Eng. Des. (manuscript submitted)

Hong, K., Barber, J.R., Thouless, M.D., Lu, W., 2018. Cracking and spalling of the oxide layer developed in high-burnup Zircaloy-4 cladding under normal operating conditions in a PWR. J. Nucl. Mater. 512, 46–55.

Johnson, A.B., Gilbert, E.R., Guenther, R.J., 1982. Behavior of spent nuclear fuel and storage system components in dry interim storage. PNL-4189, Prep. U. S. Dep. Energy under Contract DE-AC06-76RLO 1830, Pacific Northwest Lab.

Kim, H., Kim, I., Jung, Y., Park, D., Park, J., Koo, Y., 2015a. Adhesion property and high-

temperature oxidation behavior of Cr- coated Zircaloy-4 cladding tube prepared by 3D laser coating. J. Nucl. Mater. 465, 531–539.

Kim, H., Kim, I., Park, J., Koo, Y., 2015b. Application of coating technology on zirconium-based alloy to decrease high-temperature oxidation. Zircon. Nucl. Ind. 17th Vol. ASTM Int. 346–369.

Lee, Y., Lee, J.I., No, H.C., 2017. Mechanical analysis of surface-coated zircaloy cladding. Nucl. Eng. Technol. 49, 1031–1043.

Oguma, M., 1983. Cracking and relocation behavior of nuclear fuel pellets during rise to power. Nucl. Eng. Des. 76, 35–45.

Park, D.J., Kim, H.G., Jung, Y. Il, Park, J.H., Yang, J.H., Koo, Y.H., 2016. Behavior of an improved Zr fuel cladding with oxidation resistant coating under loss-of-coolant accident conditions. J. Nucl. Mater. 482, 75–82.

Park, Jung-hwan, Kim, H., Park, Jeong-yong, Jung, Y., Park, D., Koo, Y., 2015. High temperature steam-oxidation behavior of arc ion plated Cr coatings for accident tolerant fuel claddings. Surf. Coat. Technol. 280, 256–259.

Penn, W.J., Lo, R.K., Wood, J.C., 1977. CANDU fuel – power ramp performance criteria. Nucl. Technol. 34, 249–268.

Petch, N.J., 1953. The cleavage strength of polycrystals. J. Iron Steel Inst. 174, 25–28.

Rashid, Y., Dunham, R., Montgomery, R., 2004. Fuel analysis and licensing code: FALCON MOD01. EPRI Report, 1011308.

Rozzia, D., Adorni, M., Nevo, A. Del, Auria, F.D., 2011. Capabilities of TRANSURANUS code in simulating power ramp tests from the IFPE database. Nucl. Eng. Des. 241, 1078–1086.

Ševeček, M., Gurgen, A., Seshadri, A., Che, Y., Wagih, M., Phillips, B., Champagne, V., Shirvan, K., 2018. Development of Cr cold spray-coated fuel cladding with enhanced accident tolerance. Nucl. Eng. Technol. 50, 229–236.

Siefken, L.J., Coryell, E.W., Harvego, E.A., Hohorst, J.K., 2001. SCDAP/RELAP5/MOD 3.3 Code Manual: MATPRO—A Library of Materials Properties for Light-Water-Reactor Accident Analysis. Idaho Natl. Eng. Environ. Lab.

Tang, C., Stueber, M., Seifert, H.J., Steinbrueck, M., 2017. Protective coatings on zirconium-based alloys as accident-tolerant fuel (ATF) claddings. Corros. Rev. 35, 141–165.

Terrani, K.A., 2018. Accident tolerant fuel cladding development: Promise, status, and challenges. J. Nucl. Mater. 501, 13–30.

Thornley, J.C., Wronski, A.S., 1972. The grain size dependences of the failure mode and ductility transition temperatures of melted chromium and tungsten. Met. Sci. J. 6, 113–118.

Wagih, M., Spencer, B., Hales, J., Shirvan, K., 2018. Fuel performance of chromium-coated zirconium alloy and silicon carbide accident tolerant fuel claddings. Ann. Nucl. Energy 120, 304–318.

Wang, H., Hu, Z., Lu, W., Thouless, M.D., 2013. A mechanism-based framework for the numerical analysis of creep in zircaloy-4. J. Nucl. Mater. 433, 188–198.

Williamson, R.L., Hales, J.D., Novascone, S.R., Tonks, M.R., Gaston, D.R., Permann, C.J., Andrs, D., Martineau, R.C., 2012. Multidimensional multiphysics simulation of nuclear fuel behavior. J. Nucl. Mater. 423, 149–163.

Wu, A., Ribis, J., Brachet, J.C., Clouet, E., Leprłtre, F., Bordas, E., Arnal, B., 2018. HRTEM and chemical study of an ion-irradiated chromium/Zircaloy-4 interface. J. Nucl. Mater. 504, 289–299.

Yang, B., Zhang, K., Chen, G., Luo, G., Xiao, J., 2008. Measurement of fracture toughness and interfacial shear strength of hard and brittle Cr coating on ductile steel substrate. Surf. Eng. 24, 332–336.

Zinkle, S.J., Snead, L.L., 2014. Designing radiation resistance in materials for fusion energy. Annu. Rev. Mater. Res. 44, 241–267.

Appendix A. Effect of irradiation on Zircaloy and UO$_2$

A.1. Irradiation creep for Zircaloy

The equation for the irradiation creep of Zircaloy was taken from BISON (Hales *et al.*, 2016):

$$\dot{\epsilon}_{irradiation} = 1.654 \times 10^{-24} \phi^{0.85} \sigma_m, \tag{A.1}$$

where $\phi = 3 \times 10^{17}$ n/m^{2}s is the fast neutron flux and σ_m is the von Mises effective stress in MPa.

A.2. Irradiation creep for UO$_2$

Combined thermal and irradiation creep of UO2 is expressed by the following equation in MATPRO (Siefken *et al.*, 2001):

$$\dot{\epsilon} = \frac{A_1 + A_2 \dot{F}}{(A_3 + D)G^2} \sigma_m e^{-\frac{Q_1}{RT}} + \frac{A_4}{(A_6 + D)} \sigma_m^{4.5} e^{-\frac{Q_2}{RT}} + A_7 \dot{F} \sigma_m e^{-\frac{Q_3}{RT}}, \tag{A.2}$$

where $\dot{\epsilon}$ is the creep strain rate, $\dot{F}$ is the volumetric fission rate, D is the fuel density, G is the grain size in μm, Q_{1-3} are activation energies, R is the universal gas constant, T is temperature in K, and A_{1-7} are material constants.

There is a discrepancy between the part of thermal creep in MATPRO and the deformation mechanism map by Frost and Ashby (1982). We used the latter for thermal creep since it is more comprehensive. For example, it includes grain-boundary and lattice-controlled diffusion, power-law creep induced by core diffusion and lattice diffusion, and dislocation glide, which are not explicitly included in the MATPRO equation. Therefore, we implemented irradiation creep from MATPRO (terms containing the factor $\dot{F}$ in Eq. (A.2)), and thermal creep from the deformation mechanism map. The values of the non-zero irradiation creep parameters

were set to $D = 95$, $A_2 = 1.31{\times}10^{-19}$, $A_3 = -87.7$, $A_7 = 3.72{\times}10^{-35}$, $Q_1 = 3.77{\times}10^5$ J/mol,

$Q_3 = 2.62{\times}10^3$ J/mol, $\dot{F} = 1.2{\times}10^{19}$ fission/m³s.

A.3. Irradiation growth for Zircaloy

The equation for irradiation growth of Zircaloy was taken from MATPRO (Siefken *et al.*, 2001):

$$\epsilon_i = 1.407{\times}10^{-16}e^{\frac{240.8}{T}}(\phi t)^{0.5}(1 - 3f_i)(1 + 2CW), \tag{A.3}$$

where ϵ_i is the normal strain in direction i, t is time in s, f_i is the fraction of grains with the *c*-axis oriented along direction i, and CW is the reduction in the cross-sectional area caused by cold work and is set to be 0.25.

For the calculations in Section 3, isotropy was assumed based on random grain orientation of polycrystalline materials. As can be seen in Eq. (A3), irradiation growth does not cause any dimensional change in an isotropic microstructure (f_i =1/3). For the sake of argument, we therefore implemented an anisotropic microstructure with $f_r = 0.66$, $f_\theta = 0.28$, and $f_z = 0.06$ (Siefken *et al.*, 2001), to estimate the possible magnitude of irradiation growth effects.

A.4. Fuel densification

Fuel densification induced by irradiation sintering is expressed by the following equation (Rashid *et al.*, 2004):

$$\epsilon_D = \Delta\rho_0 \left[0.01\exp\left(\frac{Bu}{C_D Bu_D}\right) - 1\right], \tag{A.4}$$

where ϵ_D is the densification strain, $\Delta\rho_0$ is the total densification that can occur (a fraction of the theoretical density), Bu is the burnup, and Bu_D is the burnup at full densification, which was set

to be 5 MWd/kgU (Williamson *et al.*, 2012). C_D is a temperature-dependent parameter given by $7.2 - 0.0086(T - 298)$ for $T < 1023$ K.

Appendix B. Matlab routine demonstrating the design protocol

```matlab
% ---------------------------------------------------------------------------
% Function Name: myplot
% Purpose: solve ODE to obtain hoop and axial stresses
% Inputs: time domain, initial axial stress, initial hoop stress
% Outputs: plot of stresses vs time
% ---------------------------------------------------------------------------

function myplot(t_f,s0_a,s0_h)
s0 = [s0_a s0_h];
% Initial conditions of axial stress(s0_a) and hoop stress(s0_h)
corresponding to thermal mismatch stress
tspan = [0 t_f]; % Timespan from 0 to t_f
[t,y] = ode45(@(t,y) odefun(t,y), tspan, s0);
% ODE solver with Runge-Kutta (4,5) formula
plot(t,y(:,1),'-o',t,y(:,2),'-.') % Plot the stresses vs time
end


% ---------------------------------------------------------------------------
% Function Name: odefun
% Purpose: set up ODE based on constitutive law and creep law at time t
% Inputs: time, stresses
% Outputs: derivatives of stresses
% ---------------------------------------------------------------------------

function dydt = odefun(t,y)
% y(1) : axial stress, y(2) : hoop stress
v = 0.22; % Poisson ratio of Cr
E = 280000; % Elastic modulus of Cr

% Read strain-time data from FE calculation
fileID = fopen('strain_clad.txt','r');
% Text file 'strain_clad.txt' is indicated by the file identifier
formatSpec = '%d %f'; % Format of data fields
sizeA = [2 Inf]; % Dimensions of output array
A = fscanf(fileID,formatSpec,sizeA);

t_1 = A(1,:); % Time data
s_tot = A(2,:); % Strain data

s_int=interp1(t_1,s_tot,t); % Interpolate the data set(strain-time) at time t
s_r = -16; % Radial stress corresponding to pressure of primary coolant

dydt = zeros(2,1); % Create array for stress rates
dydt(1) = E/(1-v^2)*(s_int-crate(s_r,y(1),y(2))/vonmises(s_r,y(1),y(2))*((1-
0.5*v)*y(1)-(0.5-v)*y(2)-0.5*(1+v)*s_r));
% Equation for axial stress rate at time t
dydt(2) = E/(1-v^2)*(v*s_int-crate(s_r,y(1),y(2))/vonmises(s_r,y(1),y(2))*((v
-0.5)*y(1)-(0.5*v-1)*y(2)-0.5*(1+v)*s_r));
% Equation for hoop stress rate at time t
end
```

```matlab
% -------------------------------------------------------------------------
% Function Name: vonmises
% Purpose: calculate the von Mises stress
% Inputs: radial stress, hoop stress, axial stress
% Outputs: von Mises stress
% -------------------------------------------------------------------------

function sig_vm = vonmises(sig_rr, sig_tt, sig_zz)
% sig_rr : radial stress, sig_tt : hoop stress, sig_zz : axial stress
sig_vm = (((sig_rr-sig_tt)^2+(sig_tt-sig_zz)^2+(sig_zz-sig_rr)^2)/2)^(0.5);
% von Mises stress equation
end


% -------------------------------------------------------------------------
% Function Name: crate
% Purpose: calculate the creep strain rate
% Inputs: radial stress, hoop stress, axial stress
% Outputs: creep strain rate
% -------------------------------------------------------------------------

function creeprate = crate(sig_rr,sig_tt,sig_zz)
% sig_rr : radial stress, sig_tt : hoop stress, sig_zz : axial stress
TM=2163.0; % Melting temperature
U0=126000.0; % Shear modulus under 300K
TEMP=600; % Temperature corresponding to primary coolant
U=U0*(1.0+(TEMP-300.0)/TM*(-0.50)); % Shear modulus under current temperature
ES=vonmises(sig_rr,sig_tt,sig_zz)/(1.732); % Effective stress
GS=0.3*10.0^(-6.0); % Grain size

% Diffusional creep
DEFFD=2.8*(10.0^(-5.0))*exp(-36805.39/TEMP)+ 15.71/GS*(10.0^(-15.0))*exp(-
23093.58/TEMP);
Diffusionrate=ES*36.52*DEFFD/TEMP/(GS^2.0);

% Power-law creep
DEFFP=2.8*(10.0^(-5.0))*exp(-36805.39/TEMP)+0.0016*((ES/U)^2.0)*exp(-
23093.58/TEMP);
Powerlawrate=2.355*(10.0^25.0)*U/TEMP*DEFFP*((ES/U)^4.3);

% Dislocation glide
% Obstacle-controlled glide
if (ES < 1109.03)
GlideG=10.0^(6.0)*EXP(-71331.52/TEMP*(1.0-ES/1109.03));
else
GlideG=1.0D10;
% if ES>1109.03 GlideG is very large so it should be dominated by GlideL
end

% Lattice-resistance-controlled glide
if (ES < 2180.03)
GlideL=10.0^(11.0)*((ES/U)^2.0)*EXP(-8417.12/TEMP*(1.0-
(ES/2180.03)^0.75)^(1.333));
```

```
else
GlideL=1.0D10;
% if ES>2180.03 GlideL is very large so the stress should relax almost
instantaneously
end

% Total creep rate
Drate=GlideG;
if (GlideL < Drate)
Drate=GlideL;
end
if (Powerlawrate > Drate)
Drate=Powerlawrate;
end

creeprate = (Diffusionrate+Drate)/1.732;
% Equivalent (uniaxial) deviatoric creep strain rate
end
```
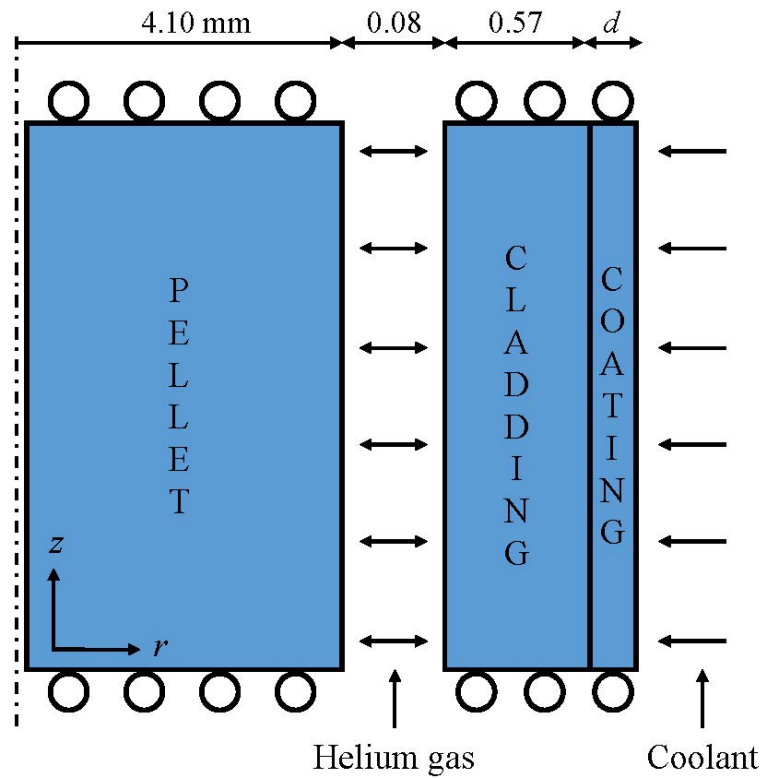
Figure 1: A 1-D, axisymmetric model of fuel assembly. Dimensions are representative of a typical fuel rod in a PWR. Various thicknesses of the Cr-coating layer d were considered in the parametric study. The displacement along the z-direction was restricted. Along the r-direction, pressure boundary conditions were imposed to account for the difference between the internal pressure induced by the helium gas and the external pressure of the primary coolant.
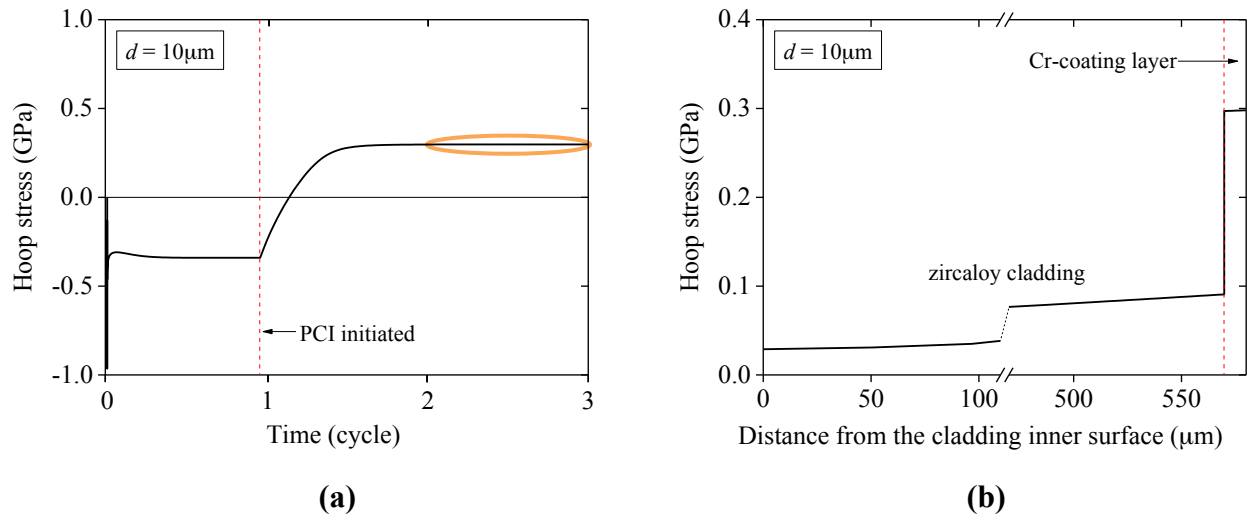
(a)

(b)

Figure 2: **(a)** Development of hoop stress at the surface of a Cr coating with a thickness of $d = 10$ μm during 3 cycles of normal operation. There are two regimes in which the stress reaches a plateau. The first, before PCI is initiated is compressive, when the rate of the creep down of the Zircaloy matches the creep rate of the Cr. The second, after PCI is initiated is tensile, when the swelling rate of the fuel matches the creep of the Cr. The onset of PCI is indicated by the dashed line just before the end of the first cycle. **(b)** The steady-state stress distribution as a function of radial position within the cladding and coating after the second plateau has been reached. The stress in the coating is essentially uniform, since the coating is much thinner than the cladding.
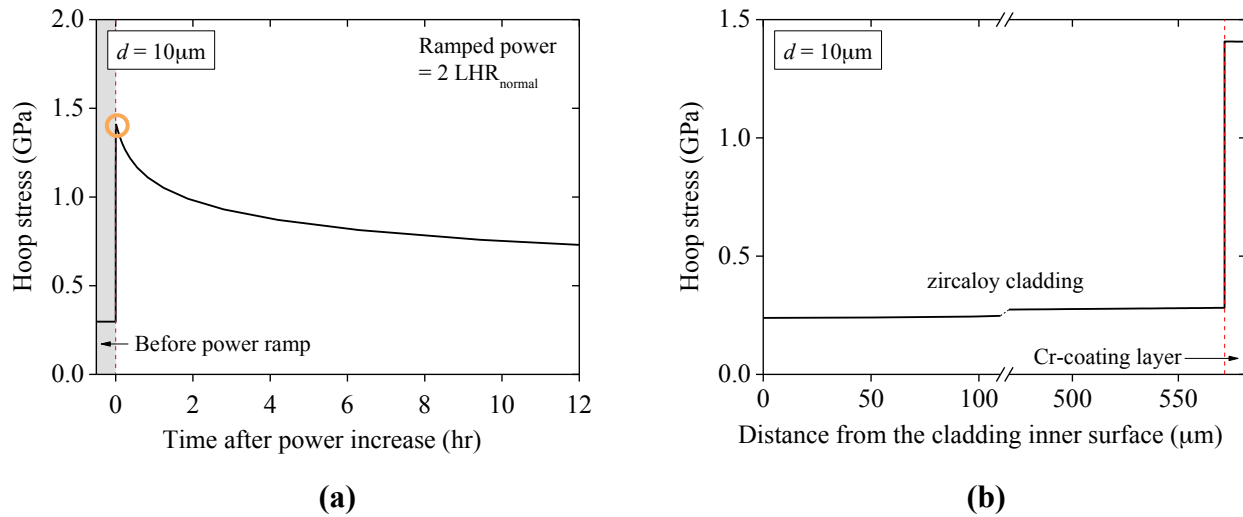
(a)

(b)

Figure 3: **(a)** Development of hoop stress in the surface of a coating layer under power ramping. The power history consists of 2 cycles of normal operation (LHR = 20 kW/m) and 12 hours of power ramp with a LHR = 40 kW/m. The shaded region shows the stress level shortly before the power ramp. **(b)** The stress distribution in the cladding and coating layer almost immediately after the power increase when the stress in the coating layer reaches a maximum, *i.e.*, the circled region in (a). The stress distribution in the coating layer is uniform along the radial direction.
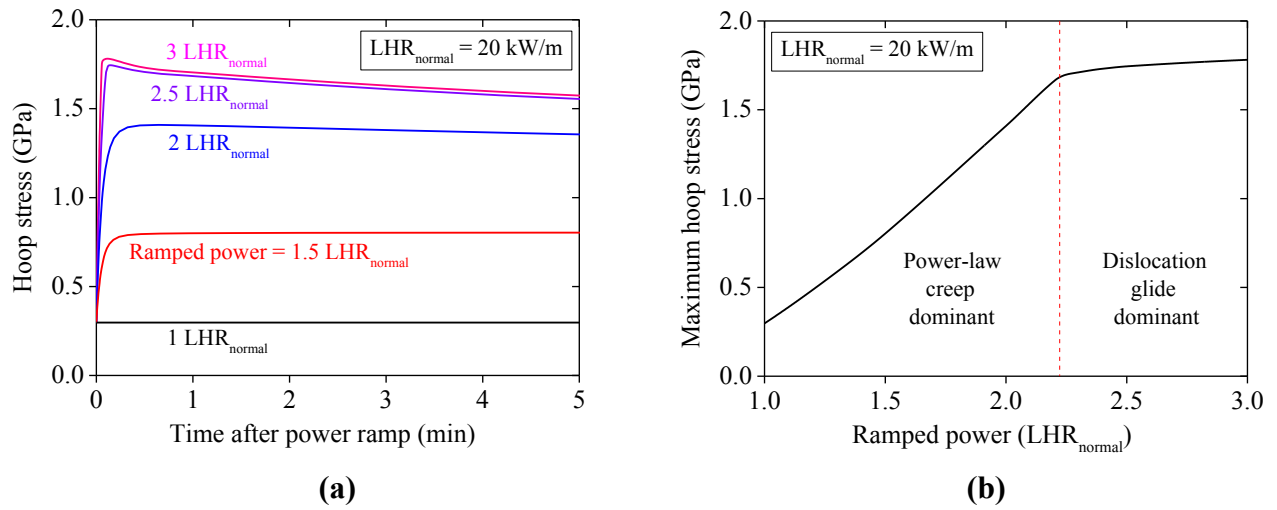
Figure 4: **(a)** Development of hoop stresses in the coating after different levels of ramped power. **(b**) The maximum hoop stresses in the coating layer after different levels of ramped power (in the multiple of LHR_{normal}). Stress relaxation is dominated by power-law creep at low ramped powers, but dominated by dislocation glide at high ramped powers. The maximum hoop stress increases with ramped power but becomes essentially independent of power when dislocation glide dominates stress relaxation.
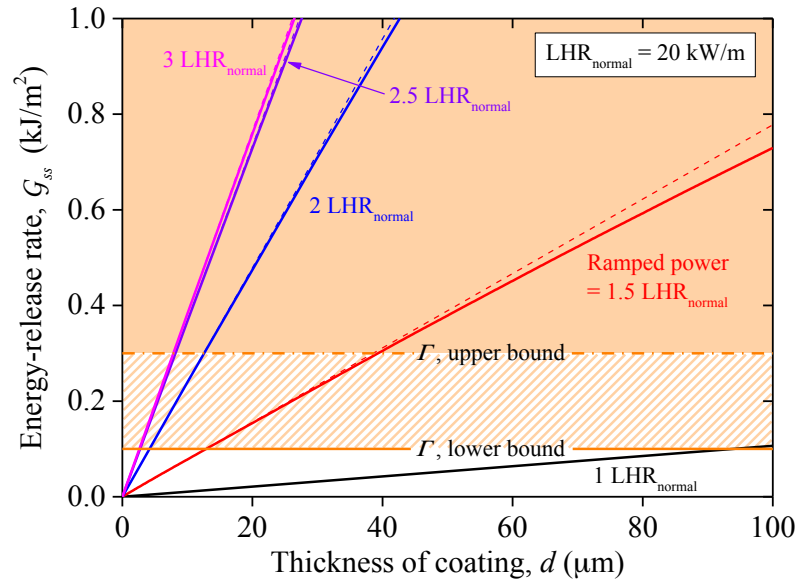
Figure 5: Steady-state energy-release rates for crack channeling as a function of coating layer thickness for different levels of ramped power. 1 LHR_{normal} corresponds to the normal operating condition. The dashed line represents the energy-release rate without considering the effect of coating layer thickness on the stress level in the layer. The hatched region between the dashed and solid line indicates a representative range for the toughness, Γ, of Cr.
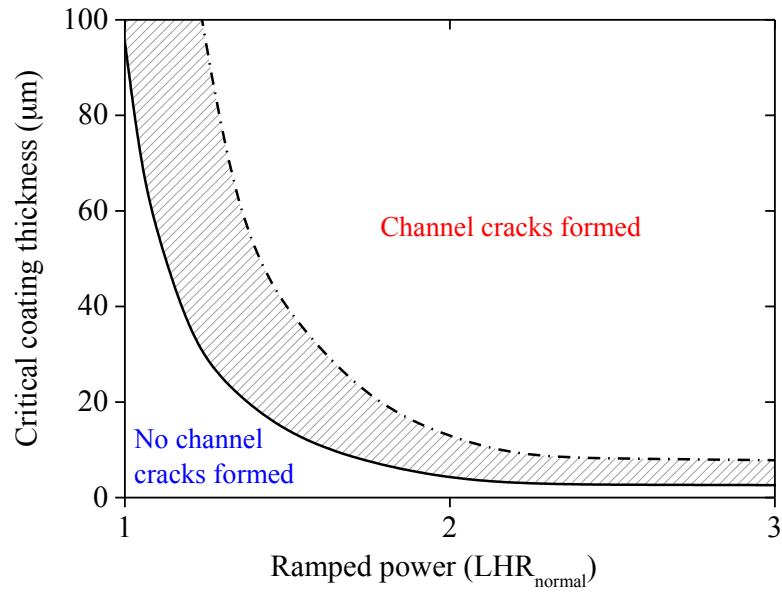
Figure 6:   Design map showing the maximum thickness of a Cr coating to avoid cracking, as a function of ramped power. The hatched region is associated with the range of fracture toughness, Γ, for Cr.